Robotica (2010) volume 28, pp. 259–265. © Cambridge University Press 2009
doi:10.1017/S0263574709990646

Development and testing of fMRI-compatible haptic interface

Ales Hribar* and Marko Munih

Faculty of Electrical Engineering, Trzaska 25, Ljubljana, Slovenija

(Received in Final Form: October 27, 2009. First published online: December 10, 2009)

SUMMARY

This paper presents the development and testing of a haptic interface compatible with a functional magnetic resonance imaging (fMRI) environment for neuroscience human motor control studies. A carbon fiber extension enables us to use the widely accepted and available haptic device Phantom 1.5.

In the first part of the paper development of the mechanical extension together with its kinematic and dynamic models are presented. The second part is focused on testing of the extended haptic interface. The experiment's results both inside and outside the fMRI environment are presented. Tests outside a scanner have shown that the mechanical extension has no notable effect on a subject performance. Experiments with the scanner have confirmed electromagnetic compatibility of the extended haptic system.

At the end it is concluded that the extended haptic device is fully compatible with the fMRI environment, and a virtual environment task that will allow neuroscientists to study a human motor control is proposed.

KEYWORDS: Haptic device; fMRI; Testing; Electromagnetic compatibility; Mechanical extension; Human motor control

1. Introduction

In the last decade, advances in functional magnetic resonance imaging (fMRI) have enabled neuroscientists to study human brain activation during basic human activities such as speaking and breathing. The fMRI technique is based on a measurement of blood-oxygen-level-dependent (BOLD) signals for estimation of neural activity in the human brain.[1] Studies[2,3] have investigated human brain activation during voluntary upper-limb movements. Controlled upper-limb movements inside an fMRI scanner could provide new, important insights into human motor control. To control and asses arm activity, a device capable of generating and measuring force and trajectories is required. An fMRI-compatible haptic interface can provide a dynamically controlled environment inside the fMRI scanner.

Any device placed inside the fMRI environment requires high level of safety and electromagnetic compatibility.[4] Three major difficulties impose limits on the use of electromechanical devices inside fMRI scanners. A high magnetic flux density, which exceeds 1 T in modern fMRI scanners, makes the use of ferromagnetic materials impossible. A high-level radio-frequency electromagnetic field and the sensitivity of the scanner receiver coils limit the use of electronic circuits. With a typical diameter of 60 cm, there is also limited space within a scanner bore. These limitations make the design of an fMRI-compatible device a challenging task.

However, a few fMRI-compatible devices have been developed in the last few years. Toma and Nakai[5] and Chapuis *et al.*[6] reported on fMRI-compatible force sensors and actuators. An fMRI-compatible surgical robot with five degrees of freedom (DOFs) for use inside an intra-operative fMRI scanner was introduced by Chinzei and Miller.[7]

Research in the field of human motor control requires a tool capable of dynamically controlling arm and hand movements inside an fMRI scanner. An fMRI-compatible hand rehabilitation device was introduced by Khanicheh *et al.*[8,9] Hydraulic, pneumatic, and ultrasonic actuators are used to drive 1-DOF haptic devices reported in refs. [10–13]. Furthermore, more sophisticated haptic devices have been described,[14,15] one of which has two DOFs and uses hydraulic actuators to generate force.[14] Another 2-DOF haptic device is powered by ultrasonic motors.[15]

However, to the best of our knowledge, no 3-DOF haptic interface has been introduced to an MRI environment to date. An important issue in fMRI experiments is the ability to imitate reality inside a scanner as closely as possible. A three-dimensional virtual environment represents a good approach. This has motivated us to modify a Phantom Premium 1.5 haptic device to be used inside an fMRI scanner room. Employing this widely accepted haptic device enabled us to use existing software, thus accelerating the designing process of the system. A mechanical carbon-fiber extension with a 3-DOF joint has been developed and coupled with the end-effector of the Phantom haptic device. This ensures that the Phantom can operate at a safe distance, well outside the high magnetic field of the main coil of an MRI scanner.

2. Extended Haptic Interface

It is believed that standard electromechanical components have no place inside an fMRI environment, as they usually contain some ferromagnetic material. In ref. [4] a definition of four zones, in which devices inside an fMRI environment may operate, is given.

The Phantom Premium 1.5 haptic device is driven by electric coreless motors. For a small electric motor operating inside an fMRI scanner room, the maximum magnetic flux density permissible is 5 mT.[16] The data supplied by Siemens

* Corresponding author. E-mail: alesh@robo.feuni-lj.si

https://doi.org/10.1017/S0263574709990646 Published online by Cambridge University Press

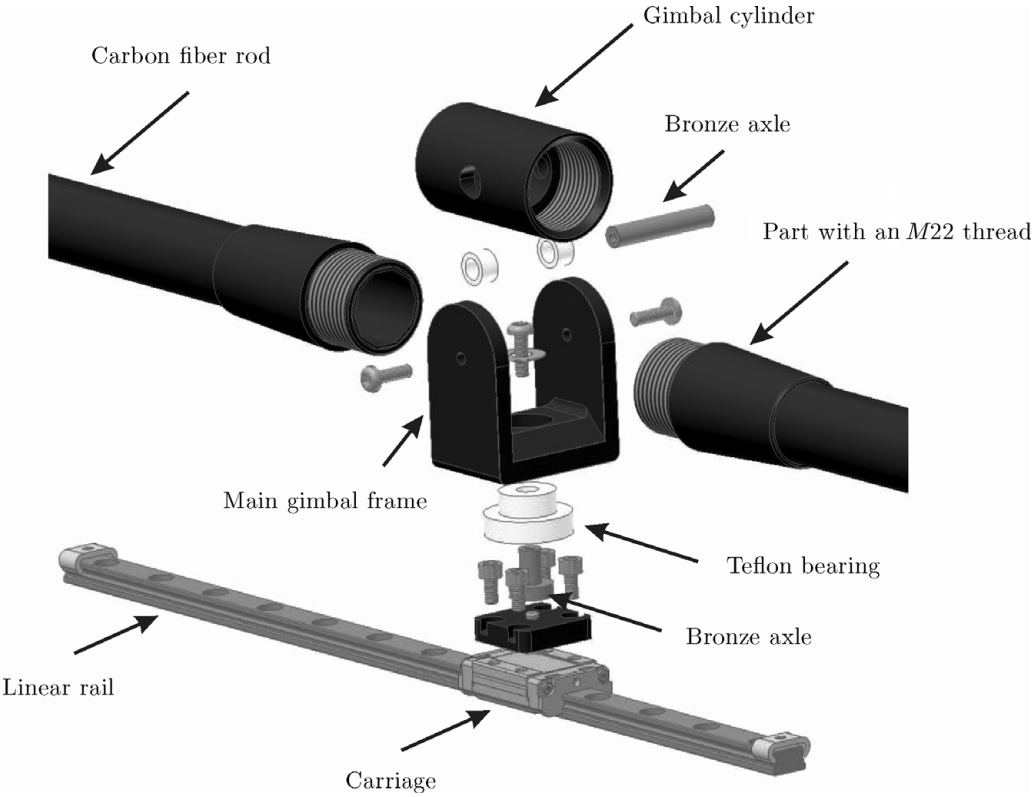


Fig. 1. Exploded view of the 3-DOF joint, which is placed in the middle of the mechanical extension. The joint consists of two rotational DOFs and one linear DOF. Note that only parts of the carbon fiber rods are shown.

suggested that the Phantom would have to be at a distance of 3 m from the isocenter of the magnet to meet this requirement. To place the Phantom's motors outside the 5-mT magnetic flux density line an extension was mounted between the end-effector of the Phantom and the subject's hand. This way the subject inside the fMRI scanner was able to manipulate the haptic device.

The mechanical extension (Fig. 1) is comprised of two carbon fiber rods, a 2-DOF gimbal, and a linear rail with a carriage. An aluminum part with an $M22\times 1.5$ thread is glued to the end of each carbon fiber rod. The rods are screwed into a gimbal cylinder, which is mounted on a main gimbal frame using a bronze axle and Teflon bearings. The main gimbal frame rotates on the bronze shaft mounted on the rail carriage. Stainless steel hex screws are used to secure both axles. Final assembly gives the mechanical extension three DOFs. The linear rail with the carriage provides a translational DOF, and the gimbal adds two rotational DOFs.

The stainless steel rail and RSR9ZM carriage were purchased from THK. The aluminum 2-DOF gimbal was designed in Autodesk Inventor (Autodesk Inc.) and manufactured in a computer numerical-controlled machine shop.

At one end the mechanical extension is coupled with the Phantom haptic device through a 3-DOF universal joint. The Phantom and the extension are fixed on an aluminum frame, which is assembled out of Bosch Rexroth aluminum strut profiles. Initially, a wooden frame was planned; however, compatibility tests (described below) demonstrated that the aluminum frame can be used inside the fMRI examination room during the experiments. Another benefit of the aluminum frame is greater mechanical robustness and a chance of easy adaptation of the haptic system to the different sizes of the subjects participating in the experiment.

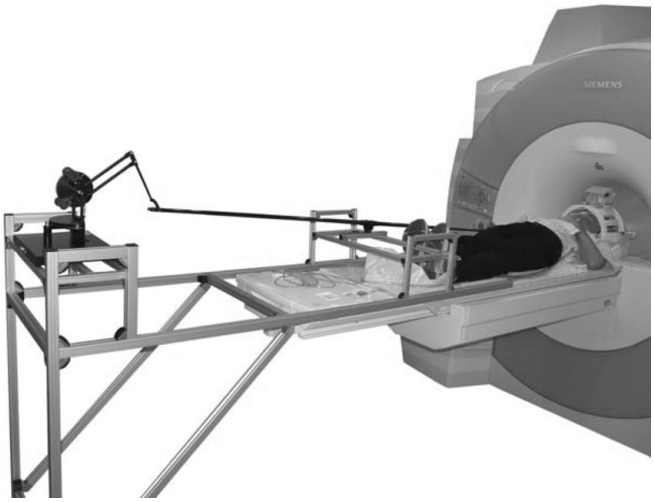


Fig. 2. Placement of the extended haptic interface inside the fMRI scanner examination room.

The aluminum frame is bolted together with stainless steel screws. A plastic part connects a sliding examination table of the fMRI scanner and the aluminum frame. The assembly is shown in Fig. 2.

A computer and a power amplifier of the Phantom are located outside the fMRI scanner examination room. To minimize the electromagnetic interference, properly shielded cables, to power and to read the Phantom motors and encoders, are placed as far away from the scanner as possible.

https://doi.org/10.1017/S0263574709990646 Published online by Cambridge University Press

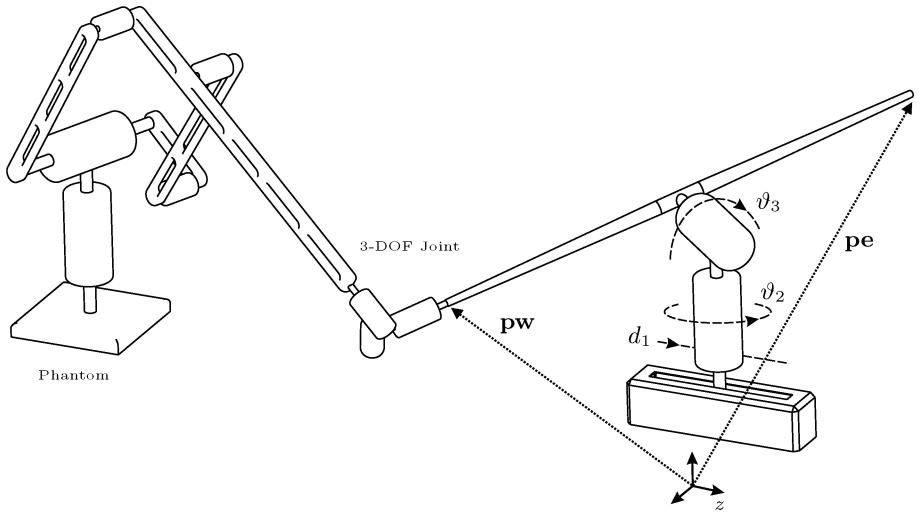


Fig. 3. Schematic view of the extended haptic device with Phantom and mechanical extension.

Table I. DH parameters.

Segment	a_i	α_i	d_i	ϑ_i
1	0	$\frac{\pi}{2}$	d_1	$\frac{\pi}{2}$
2	0	$-\frac{\pi}{2}$	0	ϑ_2
3	1	0	0	ϑ_3

2.1. Kinematics

When the extension is added to the Phantom haptic device, a kinematic map of the haptic system differs from the original Phantom kinematic model derived in ref. [17]. In Fig. 3 a schematic model of the coupled haptic system is shown. The 3-DOF joint of the mechanical extension is described by the variables ϑ_3, ϑ_2, and d_1. Denavit–Hartenberg parameters of the joint are given in Table I. These parameters are used to derive a forward kinematic matrix $T3$ equation:

$$T3 = \begin{bmatrix} -\sin(\vartheta_3) & -\cos(\vartheta_3) & 0 & -l\sin(\vartheta_3) \\ \cos(\vartheta_2)\cos(\vartheta_3) & -\cos(\vartheta_2)\sin(\vartheta_3) & -\sin(\vartheta_2) & l\cos(\vartheta_2)\cos(\vartheta_3) \\ \cos(\vartheta_3)\sin(\vartheta_2) & -\sin(\vartheta_2)\sin(\vartheta_3) & \cos(\vartheta_2) & d_1 + l\cos(\vartheta_3)\sin(\vartheta_2) \\ 0 & 0 & 0 & 1 \end{bmatrix} \tag{1}$$

As we are interested only in a positional part of the transformation the last column of the matrix $T3$ is extracted and written as a vector **pw** in Eq. (2). The system of equations (Eq. (2)) has been solved in Wolfram Mathematica considering the following assumptions: $l > 0; l > pw_x; l^2 > pw_x^2 + pw_y^2$; $-\frac{\pi}{2} \le \vartheta_2 \le \frac{\pi}{2}$ and $-\frac{\pi}{2} \le \vartheta_3 \le \frac{\pi}{2}$. An inverse kinematic map of the mechanical extension derived from **pw** is represented by Eq. (10). Results for ϑ_3, ϑ_2, and d_1 are put back into $T3$. The last column of $T3$ represents the kinematic end-to-end solution of the mechanical extension equation:

$$\mathbf{pw} = \begin{bmatrix} p_{w_x} \\ p_{w_y} \\ p_{w_z} \end{bmatrix} = \begin{bmatrix} -l\sin(\vartheta_3) \\ l\cos(\vartheta_2)\cos(\vartheta_3) \\ d_1 + l\cos(\vartheta_3)\sin(\vartheta_2) \end{bmatrix}, \tag{2}$$

$$\mathbf{q} = \begin{bmatrix} d_1 \\ \vartheta_2 \\ \vartheta_3 \end{bmatrix} = \begin{bmatrix} pw_z + \dfrac{\sqrt{l^2 - pw_x^2}\sqrt{pw_x^2 + pw_y^2 - l^2}}{\sqrt{pw_x^2 - l^2}} \\ -\arccos\left(-\dfrac{pw_y}{\sqrt{l^2 - pw_x^2}}\right) \\ -\arccos\left(-\dfrac{\sqrt{l^2 - pw_x^2}}{l}\right) \end{bmatrix}, \tag{3}$$

$$\mathbf{p}_e = \begin{bmatrix} p_{e_x} \\ p_{e_y} \\ p_{e_z} \end{bmatrix} = \begin{bmatrix} -p_{w_x} \\ -p_{w_y} \\ p_{w_z} - 2\sqrt{l^2 - p_{w_x}^2 - p_{w_y}^2} \end{bmatrix}, \tag{4}$$

2.2. Dynamics

To estimate the impact of the mechanical extension on a subject's performance during the execution of a haptic task a dynamic model of the mechanical extension has to be derived. For the linear DOF of the joint the equation

$$F = m_{ext}\ddot{z} + b\dot{z} \tag{5}$$

can be written, and for rotational joints the equation

$$M = \mathrm{i}\dot{\omega} + b\omega \tag{6}$$

can be written. When moving in the z direction, a force contributed by the extension can be calculated by Eq. (5),

https://doi.org/10.1017/S0263574709990646 Published online by Cambridge University Press

where m_{ext} is mass of the moving parts of the extension and b is a coefficient of friction. Because the frictional force is small (less than 0.01 N) compared with the force of inertia we can discard the frictional contribution.

For movement in the x and y directions a torque contributed by two rotational DOFs can be estimated by Eq. (6). The torque generated by friction in both rotational DOFs is within 10^{-3} N m; therefore it can be discarded.

Mass and mass moments of inertia (I_{ext}) of the mechanical extension were first estimated using the Autodesk Inventor physical iProperties dialog box. The mass value acquired by the Autodesk Inventor was compared with the mass measured by a precision weighing machine. The difference between these two mass values was less than 1%. In all calculations, the mass value measured with the precision weighing machine is used:

$$m_{ext} = 204 \times 10^{-3} \text{ kg}, \tag{7}$$

$$I_{ext} = \begin{bmatrix} 3.13 & 0 & 0 \\ 0 & 3.13 & 0 \\ 0 & 0 & 0 \end{bmatrix} \times 10^{-2} \text{ kg m}^2. \tag{8}$$

Planar bending of the carbon fiber extension is described by a Bernoulli–Euler beam model equation, Eq. (9), derived in ref. [18]:

$$\mathbf{B} = \begin{bmatrix} c_0 & lc_1 & ac_2 & alc_3 \\ \beta^4 c_3/l & c_0 & ac_1/l & ac_2 \\ \beta^4 c_2/a & \beta^4 lc_3/a & c_0 & lc_1 \\ \beta^4 c_1/al & \beta^4 c_2/a & \beta^4 c_3/l & c_0 \end{bmatrix}, \tag{9}$$

where

$$\beta^4 = \omega^2 l^4 \mu/(EI), \quad a = l^2/(EI),$$

$$c_0 = (\cosh\beta + \cos\beta)/2, \quad c_1 = (\sinh\beta + \sin\beta)/(2\beta),$$

$$c_2 = (\cosh\beta - \cos\beta)/(2\beta^2), \quad c_3 = (\sinh\beta - \sin\beta)/(2\beta^3),$$

$l = 1.05$ m (length),

with $\mu = 0.055$ kg/m (density/unit length),

$E = 125$ GPa (elastic modulus),

$I = \frac{\pi}{64}(D^4 - d^4) = 1.61 \times 10^{-9}$ m^4 (cross-sectional moment of inertia).

Matrix $\mathbf{B}$ relates the variables in the x and y directions at two ends of the carbon fiber extension equation, Eq. 10. In the z direction an infinite stiffness is presumed:

$$\begin{bmatrix} p_{e_{x,y}} \\ \psi_{e_{x,y}} \\ M_{e_{x,y}} \\ F_{e_{x,y}} \end{bmatrix} = \mathbf{B} \cdot \begin{bmatrix} p_{w_{x,y}} \\ \psi_{w_{x,y}} \\ M_{w_{x,y}} \\ F_{w_{x,y}} \end{bmatrix} = \begin{bmatrix} \text{displacment} \\ \text{angle} \\ \text{torque} \\ \text{force} \end{bmatrix}. \tag{10}$$

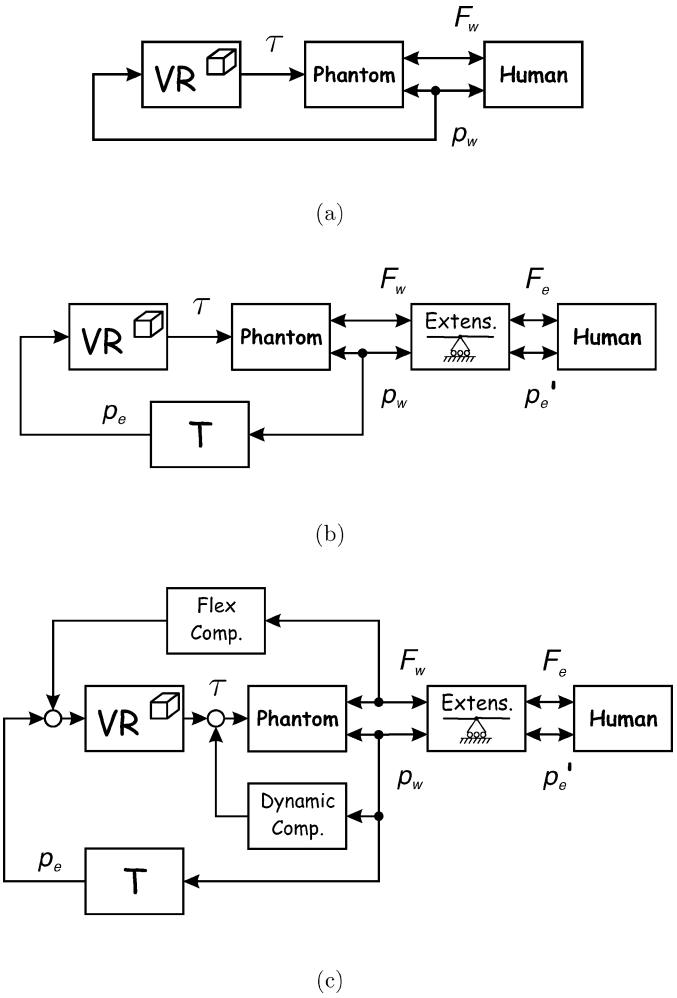


Fig. 4. Control schemes for different configurations of the haptic device: (a) only the Phantom haptic device, (b) extended haptic system without compensation, (c) extended haptic system with compensation.

2.3. Control

In most standard applications an impedance control scheme as given in Fig. 4(a) is used to guide the Phantom haptic device. When the mechanical extension is coupled with the Phantom, additional dynamics are added to the haptic system. To compensate the dynamics of the mechanical extension a control scheme in Fig. 4(c) has been used. The impedance controller in Fig. 4(b) was upgraded with two additional control blocks. A flex compensation block is used to compensate the difference between the actual and the calculated position caused by a flexion of the carbon fiber rod. When a human interacts with a rigid virtual reality (VR) object (e.g., wall) the actual position of the extension's end ($\mathbf{p}_e^{|}$) differs from the calculated one ($\mathbf{p}_e$ in Eq. (4)). To set proper motor torques (τ) in a VR block the actual position $\mathbf{p}_e^{|}$ is required. As it is not possible to directly measure the actual position $\mathbf{p}_e^{|}$ the Bernoulli–Euler beam model is employed for its estimation.

A dynamic compensation block is a feed-forward controller that compensates the forces that are caused by the movement of the mechanical extension in the free space of the virtual environment.

https://doi.org/10.1017/S0263574709990646 Published online by Cambridge University Press

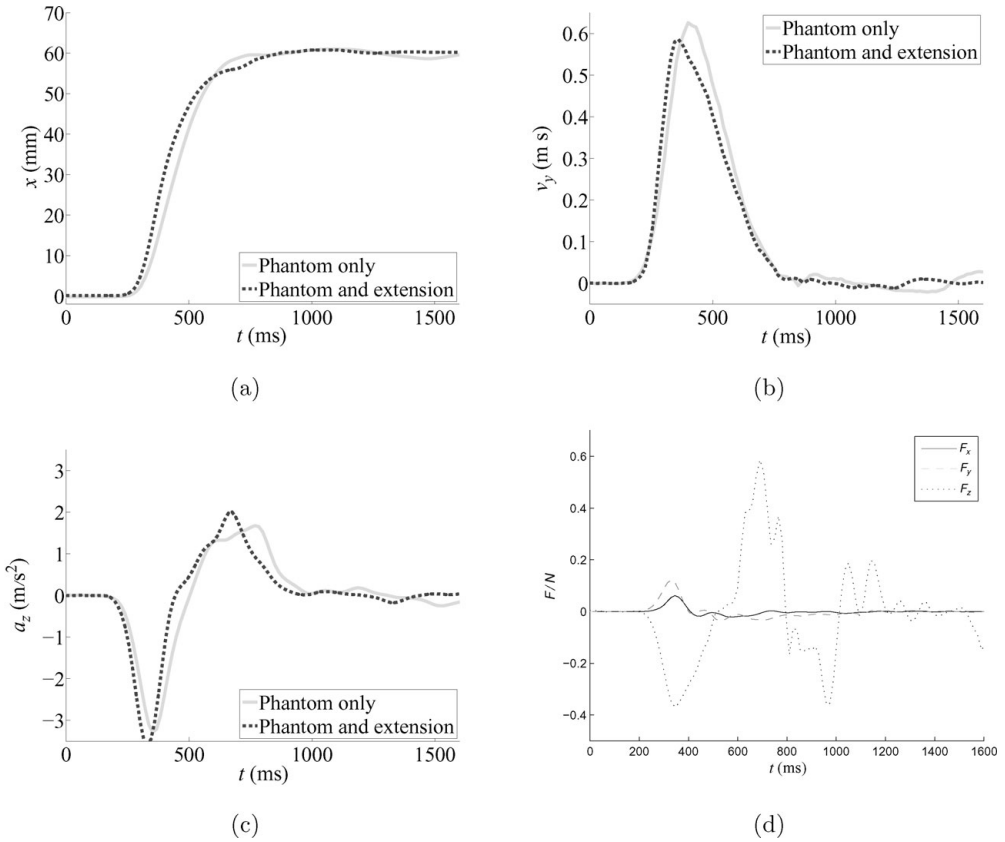


Fig. 5. Comparison of the (a) trajectories, (b) velocities, and (c) accelerations with (dashed line) and without (full line) the mechanical extension during evaluation of the reaching task outside the MRI scanner. (d) Forces induced by the mechanical extension. The coordinate system is marked in Fig. 3.

3. Evaluation and Testing

3.1. Testing outside the scanner

3.1.1. Procedure. The first experiment with the Phantom coupled with the mechanical extension was carried out in a controlled environment outside the fMRI scanner. The aim of this experiment was to asses the impact of the mechanical extension on the performance of a subject during the execution of a virtual environment task. A virtual environment task where the subject had to reach for a white square target on a back wall of a virtual environment room was programmed.

The experiment comprised two parts. Each of the five male subjects (age range 26–29 years) first executed the virtual environment task using only the Phantom haptic device. In the second part of the experiment, the mechanical extension was added to the Phantom, and the same task was repeated. A log file containing the trajectories, forces, and start and hit times for each subject was generated for every run. The data from these two experimental sets allowed us to study the effect of the mechanical extension on the trajectories, velocities and forces, and reaction times of the subject while performing the virtual environment task.

3.1.2. Results. A comparison of reaching trajectories, velocities, and accelerations with and without the mechanical extension is presented in Figs. 5(a)–5(c), respectively. Each trace represents an average of 20 trajectories captured from one subject. For demonstration purposes and clarity, only one coordinate is presented in each plot: x for trajectories, y for velocities, and z for accelerations.

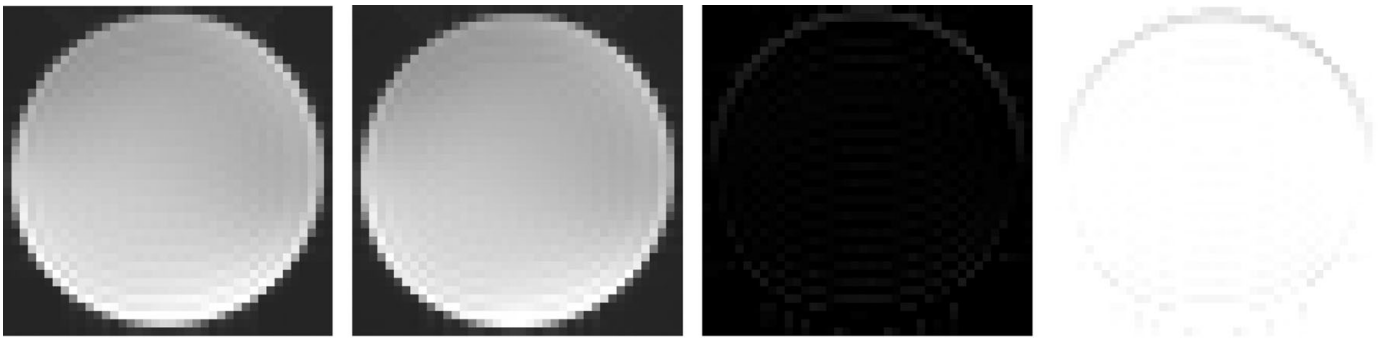
Because the virtual environment task requires no interaction forces, when the subject moves the cursor in free space of the virtual environment room, the Phantom motors do not generate any torque. When the Phantom is used without the extension, actual interaction forces with the subject are a result of the Phantom dynamics derived in refs. [19 and 20]. Use of the mechanical extension changes these interaction forces because of the difference in the dynamic model. Figure 5(d) presents the interaction forces (in all three directions) caused only by the extension.

The experiment showed that the use of the mechanical extension has a negligible effect on the subject's performance while executing the virtual environment task. Forces caused by the mechanical extension are small enough so that they do not have significant impact on reaction and movement times. Comparison of these times is given in Table II. Reaction time is the time between the moment when the white square target is shown on the screen and the moment when the

Table II. Values of reaction and movement times in milliseconds are given as the mean (standard deviation).

Mode	$T_{Reaction}$	$T_{Movement}$	T_{Total}
Phantom only	310 (33)	770 (236)	1080 (248)
Haptic system	315 (36)	780 (231)	1095 (244)

https://doi.org/10.1017/S0263574709990646 Published online by Cambridge University Press



(a) Reference image (b) Phantom running (c) Subtraction (d) Inverse image

Fig. 6. The fMRI images of the cylindrical imaging object during compatibility experiment: (a) when no haptic device was present inside examination room, (b) when haptic device was present and running inside examination room, (c) subtraction of (a) and (b), (d) inverse image of (c).

subject starts to move the cursor. Movement time is the time in which the subject is moving the cursor towards the target. Total time is the sum of movement and reaction times. The data in Table II is an average of all the times of the five subjects who participated in the experiment.

3.2. Test of electromagnetic compatibility

3.2.1. Procedure. The experiments described below were carried out to demonstrate the compatibility of the extended haptic system with a 3-T Siemens MAGNETOM Trio fMRI scanner, of the University Medical Center Ljubljana, Slovenia. All experiments with the fMRI scanner included trained personnel.

Before the Phantom haptic device was taken inside the fMRI examination room, the distribution of a static magnetic field of the scanner was studied. With the static magnetic field model supplied by Siemens we were able to determine the approximate position of the Phantom inside the examination room. Additional measurements of the magnetic flux density (**B**) showed that the Phantom would need to be at a distance of 3 m from the isomagnetic center of the fMRI scanner, to satisfy the maximum allowed flux density in which the electric motors of the Phantom may operate.

In the next step, possible interference of the Phantom operation inside the examination room during fMRI was observed. All tests were carried out on the same day using echo planar imaging sequences, which are commonly used in brain fMRI examinations. Sequence parameters were fixed throughout the experiments (T_R = 3000 ms, T_E = 30 ms, field of view = 192 mm, 36 slices, slice thickness 6 mm, voxel size 3 × 3 × 3 mm^3). A cylindrical imaging object (plastic bottle 1900 mL, per 1000 g H_2O dist.: 3.75 g $NiSO_4$ × $6H_2O$ + 5 g NaCl) was placed inside the scanner. The first set of images was acquired without the Phantom inside the examination room. Then the Phantom was placed on the previously determined spot (described above) inside the examination room (Fig. 2). The phantom was connected to the amplifiers, which were placed outside the room, and the virtual environment task was ran. The subject inside the examination room was executing the task while another set of images was acquired.

3.2.2. Results. The acquired images were analyzed in MATLAB as proposed in ref. [21]. A mean pixel value of 30 images of slice 18/36 for both image sets was first calculated (IMAGE1 and IMAGE2). Then a pixel-by-pixel difference image was acquired (IMAGE3).

Standard deviation (SD) of the pixel values within the measurement region of interest (MROI) on IMAGE3 was determined (Eq. (11)). The MROI extended over 80% of the cylindrical imaging object cross-sectional area:

$$\mathrm{SD} = \sqrt{\frac{\sum_{i=1}^{n}\sum_{j=1}^{m}(V(i,j)-\overline{V})^2}{2\sum_{i=1}^{n}(m_i-1)}} \tag{11}$$

In Eq. (11), $V(i, j)$ denotes pixel value in IMAGE3, while $\overline{V}$ is the average pixel value. Image noise (IMN) was calculated as

$$\mathrm{IMN} = \frac{\mathrm{SD}}{\sqrt{2}} \tag{12}$$

Image signal (S) was determined as mean pixel value within the MROIs of IMAGE1 and IMAGE2. A signal-to-noise ratio (SNR) (Eq. (13)) was calculated for both cases. When no haptic device was present inside the examination room the SNR was 172. For haptic device present and operating inside the examination room the SNR was 171:

$$\mathrm{SNR} = \frac{\mathrm{S}}{\mathrm{IMN}}. \tag{13}$$

Figures 6(a)–6(d) present acquired images during compatibility experiment. In Fig. 6(a) the mean value of first imaging set (30 images of slice 18/36, reference imaging, IMAGE1) is shown. Figure 6(b) shows the mean value of the second imaging set (30 images of slice 18/36, haptic device running inside examination room, IMAGE2). Subtraction of the images in Figs. 6(a) and 6(b) is shown in Fig. 6(c)—IMAGE3. An inverse of IMAGE3 is presented in Fig. 6(d).

In Fig. 6(c) a slight shift of the subtracted images can be observed. This "ring effect," which can be seen even better in Fig. 6(d), has also been reported in refs. [7, 9, and 11]. It is not clear whether shift was caused by the haptic device running inside examination room or by a spatial shift of the imaging object while two sets of fMRI images were acquired. However the SNR of the images acquired during the Phantom

https://doi.org/10.1017/S0263574709990646 Published online by Cambridge University Press

operation is still high enough for us to be able to use them to determine regions of brain activation.

4. Discussion and Conclusion

In this paper the upgrade of the Phantom haptic device has been presented. The upgrade enables the Phantom to operate inside the fMRI examination room. Comprehensive study has demonstrated that it is possible to use the Phantom haptic device together with the mechanical extension inside the fMRI environment.

Tests in laboratory showed that for a simple virtual environment tasks the mechanical extension does not have significant impact on haptic perception. Because of its light weight and small mass moments of inertia, dynamic forces contributed by mechanical extension are small enough that they do not have a notable effect on the subject's performance during the execution of the virtual environment task. This was also confirmed by comparison of movement times with and without the extension.

Experiments with the fMRI scanner have also confirmed electromagnetic compatibility of the extended haptic device with the fMRI environment. Analysis of fMRI images acquired during the operation of the haptic device inside the scanner examination room revealed the SNR of these images to be 171. With images of such quality neurophysiologists are able to determine regions of human brain activation during different controlled, motor-oriented arm movements.

We believe that as long as interaction forces are in a range of a few Newtons, this method can be applied to many different types of haptic devices (such as Fokker Haptic Master[22] and MIT Manus[23]), thus enabling them to work inside the fMRI environment.

Future work will include development and programming of a virtual environment in which a human subject will perform reaching movements. Extended haptic interface will be used for what it was designed. This combination of virtual environment and haptic system together with the fMRI technique will allow neurophysiologists to start a new chapter in the study of human motor control.

References

1. S. Ogawa, R. S. Menon, S. G. Kim and K. Ugurbil, "On the characteristics of functional magnetic resonance imaging of the brain," *Annu. Rev. Biophys. Biomol. Struct.* **27**, 447–474 (1998).
2. S. Lehericy, E. Bardinet, L. Tremblay, P. F. Van de Moortele, J. B. Pochon, D. Dormont, D. S. Kim, J. Yelnik and K. Ugurbil, "Motor control in basal ganglia circuits using fMRI and brain atlas approaches," *Cerebr. Cort.* **16**, 149–161 (2006).
3. K. Toma and T. Nakai, "Functional MRI in human motor control studies and clinical applications," *Magnet. Reson. Med. Sci.* **1**, 109–120 (2002).
4. B. A. Schueler, T. B. Parrish, J. C. Lin, B. E. Hammer, B. J. Pangrle, E. R. Ritenour, J. Kucharczyk and C. L. Truwit, "MRI compatibility and visibility assessment of implantable medical devices," *J. Magnet. Reson. Imag.* **9**, 596–603 (1999).
5. D. Chapuis, R. Gassert, L. Sache, E. Burdet and H. Bleuler, "Design of a Simple MRI/fMRI Compatible Force/Torque Sensor," *Proceedings of the 2004 IEEE/RSJ International Conference on Intelligent Robots and Systems*, Sendai, Japan (Sep. 28–Oct. 2, 2004).
6. J. Vogan, A. Wingert, J. S. Plante, S. Dubowsky, M. Hafez, D. Kacher and F. Jolesz, "Manipulation in MRI Devices Using Electrostrictive Polymer Actuators with an Application to Reconfigurable Imaging Coils," *Proceedings of the 2004 IEEE International Conference on Robotics and Automation*, New Orleans, LA, USA (Apr. 26–May 1, 2004).
7. K. Chinzei and K. Miller, "MRI Guided Surgical Robot," *Proceedings of the 2001 Australian Conference on Robotics and Automation*, Sydney, Australia (Nov. 14–15, 2001).
8. A. Khanicheh, A. Muto, C. Triantafyllou, B. Weinberg, L. Astrakas, A. Tzika and C. Mavroidis, "fMRI-compatible rehabilitation hand device," *J. NeuroEng. Rehab.* **3**, 24 (2006).
9. A. Khanicheh, D. Mintzopoulos, B. Weinberg, A. Tzika and C. Mavroidis, "MR_CHIROD v.2: A fMRI Compatible Mechatronic Hand Rehabilitation Device," *Proceedings of the 10th IEEE International Conference on Rehabilitation Robotics*, Noordwijk, The Netherlands (Jun. 12–15, 2007).
10. M. Flueckiger, M. Bullo, D. Chapuis, R. Gassert and Y. Perriard, "fMRI Compatible Haptic Interface Actuated with Traveling Wave Ultrasonic Motor," *Proceedings of the 2005 Industry Applications Conference, 40th IAS Annual Meeting*, Vol. 3 (2005) pp. 2075–2082.
11. N. Yu, W. Murr, A. Blickenstorfer, S. Kollias and R. Riener, "An fMRI Compatible Haptic Interface with Pneumatic Actuation," *Proceedings of the 10th IEEE International Conference on Rehabilitation Robotics*, Noordwijk, The Netherlands (Jun. 12–15, 2007).
12. R. Gassert, R. Moser, E. Burdet and H. Bleuler, "MRI/fMRI-compatible robotic system with force feedback for interaction with human motion," *IEEE/ASME Trans. Mechatron.* **11**, 216–224 (2006).
13. N. Yu, C. Hollnagel, A. Blickenstorfer, S. S. Kollias and R. Riener, "Comparison of MRI-compatible mechatronic systems with hydrodynamic and pneumatic actuation," *IEEE/ASME Trans. Mechatron.* **13**, 268–277 (2008).
14. R. Gassert, L. Dovat, O. Lambercy, Y. Ruffieux, D. Chapuis, G. Ganesh, E. Burdet and H. Bleuler, "A 2-DOF fMRI Compatible Haptic Interface to Investigate the Neural Control of Arm Movements," *Proceedings of the 2006 IEEE International Conference on Robotics and Automation*, Orlando, FL, USA (May 15–19, 2006).
15. J. Izawa, T. Shimizu, T. Aodai, T. Kondo, H. Gomi, S. Toyama and K. Ito, "MR Compatible Manipulandum with Ultrasonic Motor for fMRI Studies," *Proceedings of the 2006 IEEE International Conference on Robotics and Automation*, Orlando, FL, USA (May 15–19, 2006).
16. SIEMENS Medical Solutions, "MAGNETIC RESONANCE MAGNETOM Trio: A Tim System," Technical Drawing (2006).
17. M. C. Cavusoglu and D. Feygin, "Kinematics and dynamics of Phantom model 1.5 haptic interface," *Presence: Teleop. Virtual Environ.* **11**(6), 327–343 (2002).
18. E. C. Pestel and F. A. Leckie, *Matrix Methods in Elastomechanics* (McGraw-Hill, New York, 1963).
19. A. M. Tahmasebi, B. Taati, F. Mobasser and K. H. Zaad, "Dynamic Parameter Identification and Analysis of a Phantom Haptic Device", *Proceedings of the 2005 IEEE Conference on Control Applications*, Toronto, Canada (Aug. 28–31, 2005).
20. M. C. Cavusoglu, D. Feygin and F. Tendick, "A critical study of the mechanical and electrical properties of the phantom haptic interface and improvements for high performance control," *Presence: Teleop. Virtual Environ.* **11**(5), 555–568 (2002).
21. NEMA, "Determination of Signal-to-Noise Ratio (SNR) in Diagnostic Magnetic Resonance Imaging," Standards Publication MS 1-2001, (May 8, 2008). Available at http://www.nema.org/stds/ms1.cfm#download
22. W. Harwin and M. Hillman, "Introduction," *Robotica* **21**(1), 1 (2003).
23. H. I. Krebs, B. T. Volpe, M. L. Aisen, W. Hening, S. Adamovich, H. Poizner, K. Subrahmanyan and N. Hogan, "Robotic applications in neuromotor rehabilitation," *Robotica* **21**(1), 3–11 (2003).

https://doi.org/10.1017/S0263574709990646 Published online by Cambridge University Press